MEMS-based power disconnect for 42-V automotive power systems

Henry K. Chu
James K. Mills
William L. Cleghorn
University of Toronto
Department of Mechanical and Industrial
    Engineering
5 King's College Road
Toronto, Ontario, Canada M5S 3G8
E-mail: chu@mie.utoronto.ca

Abstract. We present the design of a micro-electro-mechanical-system (MEMS)–based power disconnect for use with the proposed 42-V automotive power systems. High-voltage power systems are prone to arcing, which occurs during power disconnections. The high arcing current may lead to severe damage on the systems and may expose electric shock hazards to humans. The objective of the MEMS-based power disconnect we propose is to eliminate arcing occurrence in the systems. To eliminate arcing, one alternative is to electronically terminate the power supply to the system prior to the physical disconnection. The integrated MEMS force sensor on the power disconnect will be activated as a service technician disconnects the connector. The power supply to the system will be electronically shut off to prevent arcing during the physical interruption. The MEMS force sensor on the disconnect has an overall dimension of $3600~\mu\text{m} \times 1000~\mu\text{m} \times 10~\mu\text{m}$ and is fabricated with the Micragem fabrication process. A displacement reduction mechanism is incorporated into the sensor design to increase the sensitivity of the force sensor. Results show that the sensor is capable of measuring a maximum force input of 10.7 mN, resulting from a 20-μm displacement on the sensing structure. © *2008 Society of Photo-Optical Instrumentation Engineers.*
[DOI: 10.1117/1.2896107]

Subject terms: microelectromechanical systems; sensors; integrated circuits; noise.

1 Introduction

From indicator lights on a dashboard and power door locks to more advanced antilock braking systems and traction control systems, the battery in an automotive vehicle is the sole power source to all of the electrical components and devices inside the vehicle. However, as more and more of these electrical devices have been installed onto the vehicle, the battery power demand has gradually increased. The present 200 A/3 kW, 14-V battery systems will soon be insufficient to satisfy increasing automobile power demands. Hence, the automotive industry proposes increasing the battery voltage from 14 V to 42 V for the next-generation vehicle. This new battery standard will be capable of providing electrical power up to 200 A/9 kW. However, one major challenge with such a high battery voltage is that there will be an increased possibility of arc discharge during physical connection and disconnection of electrical devices in the vehicle. The high arc discharge current may cause severe damage to the terminals and the systems and may pose electric shock hazards to humans.[1,2] To resolve the problem, a micro-electro-mechanical-system (MEMS)–based power disconnect system is proposed.

MEMS devices have become one of the fastest growing products in the automotive industry. The advantages of such devices are their small physical size and low power consumption. Many modern vehicles are now installed with MEMS devices to enhance the comfort and safety of the

vehicles. For instance, MEMS-based pressure sensors may be installed in the tire pressure monitoring system (TPMS) to consistently monitor the pressure level inside the tire. MEMS-based accelerometers may be found in some airbag deployment systems for crash detection.[3]

The power disconnect system proposed in this paper consists of a MEMS sensor, a readout circuit, and a relay. Figure 1 shows a schematic of the power disconnect system. The MEMS sensor may be installed onto the custom-made package cover described in Ref. 4. The cover serves as an interface for the force input as well as a mechanism to transform the macroscopic input force imparted by a service technician into a fine motion on the order of a few microns to be applied to the sensor. Preliminary results show that a grasping displacement of 30.86 μm will result in response to a 60-N macroscopic force input.[4] In the presence of human contact, the disconnect system will trigger a signal to an electronic relay to electronically terminate the power supply to the electric load. As a result, arcing will not occur during the physical interruption of the connector terminals.

The MEMS sensor installed on the power disconnect system is a capacitive-type force sensor. The capacitive sensing principle is selected for this MEMS-sensor application because of its simple structure, high sensitivity, low temperature dependence, and low power consumption.[5] Over the past several years, researchers have investigated different capacitive-type sensors for force and strain measurement. Despont et al.[6] micromachined a capacitive force sensor. This sensor could measure force between 0.01 N
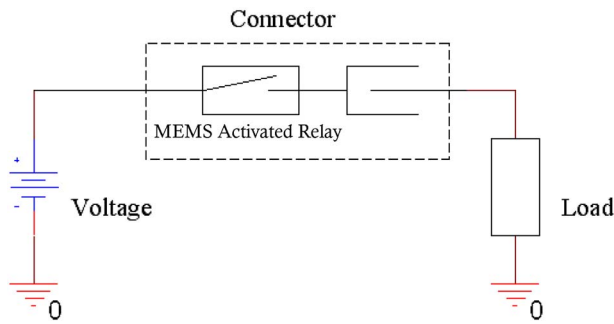
Fig. 1 Schematic of the MEMS-based power disconnect system.

Fig. 2 Schematic of the sensor: (a) top view; (b) side view.

and 10 N. The differential configuration of the comb-fingers in the sensor helped to improve linearity and sensitivity. Sun et al.[7] proposed a capacitive 2-degrees of freedom (DOF) force sensor for micro-force measurement. The group used six sets of comb drives in an orthogonal arrangement to resolve forces in the *x* and *y* directions. Aebersold et al.[8] published a capacitive sensor design for bending strain measurement. Experimental results showed that this version of capacitive sensor was capable of detecting over 1600-$\mu\varepsilon$ strain. In general, the preceding capacitive sensor designs employ the space-variation type capacitive sensing principle. This principle has the advantage of providing high output capacitance. However, the sensitivity tends to decrease as the force or displacement to be measured increases. To resolve this issue, a MEMS-based, high-sensitivity, capacitive sensor is proposed in this paper.

This paper mainly presents the design of a MEMS-based capacitive sensor and its associated readout circuitry for high-sensitivity force detection. Section 2 provides a description of the sensor design and its fabrication process. Modeling equations of the capacitive force sensor are presented in Sec. 3. Section 4 describes the details regarding the design of the readout circuit. Results from the signal noise analysis conducted in this study are discussed in Sec. 5. Design of the experiments and the results will be covered in Sec. 6. The last section of this paper summarizes the results and findings obtained from this study.

2 MEMS Capacitive Force Sensor

2.1 Sensor Architecture

Figure 2 shows the architecture of the proposed MEMS-based space-variation type capacitive force sensor. Details of the development of this sensor design are described in Ref. 9. The overall dimensions of the entire MEMS sensor structure are 3600 μm × 1000 μm. The sensor consists of two identical comb-drive mechanisms (labeled #1 and #2) located at the center part of the sensor, as shown in Fig. 2(a). The comb-drive mechanisms will alter the sensor capacitance in response to an external force imparted onto the sensor.

This design of the capacitive force sensor also incorporates a displacement reduction mechanism. The outer structure of the sensor in Fig. 2(a) is the displacement reduction mechanism. The mechanism is designed to convert the imparted displacement from the input force in the vertical direction to a smaller lateral displacement onto the comb-
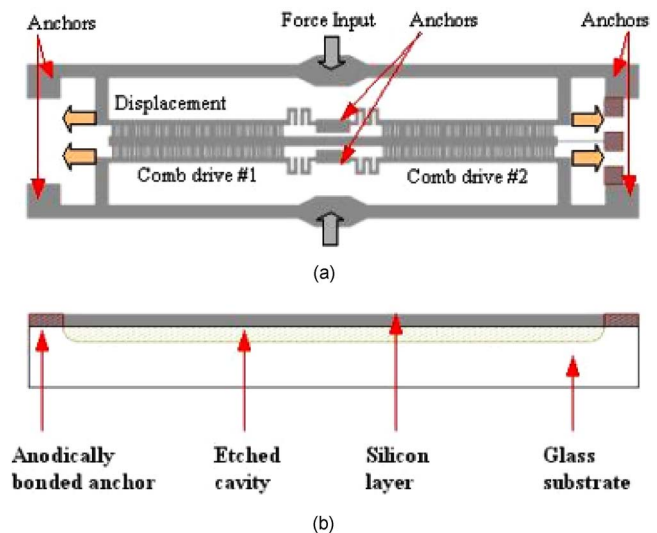
drive mechanisms. The presence of such a mechanism helps prevent damage of the comb-drive mechanism and improves the sensor sensitivity.

2.2 Comb-Drive Mechanism

Each of the two comb-drive mechanisms consists of 59 sets of movable electrodes for force sensing. Each comb-finger is 60 μm in length and 4 μm in width, with an overlapping area of 560 μm^2. The comb-drive mechanisms detect the input force imparted onto the sensor through the changes in the air gap between the comb-fingers. When a force is applied vertically onto the top and bottom beams of the sensor structure, the comb drive will experience a reduced relative motion in the lateral direction, as illustrated in Fig. 2(a). As a result, the gap between the comb-fingers changes, as illustrated in Fig. 3. Due to the differential comb-drive configuration employed in this sensor, the capacitance value on one side decreases while the capacitance value on the other side increases. By measuring the change in the capacitance value, the applied force can be determined. Details of the detection principle will be discussed subsequently.
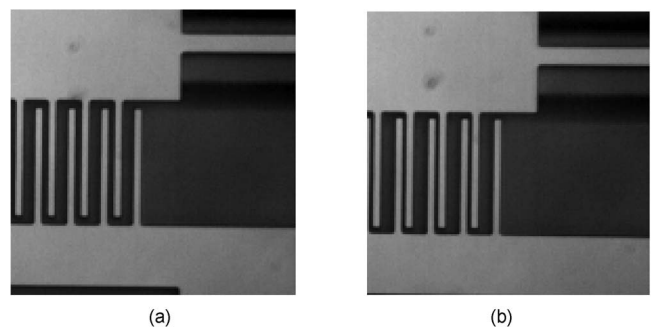

Fig. 3 Details of the force sensors illustrating the capacitance decrease due to a force input: (a) sensor at original position; (b) sensor at new position.
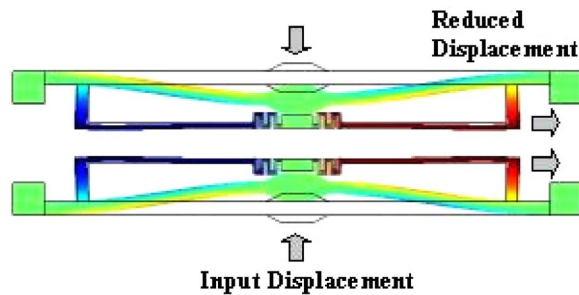
Fig. 4 Schematic of the displacement reduction mechanism.

Fig. 6 Image of the MEMS sensor under an optical microscope.

2.3 Displacement Reduction Mechanism

Motion amplification mechanisms are often incorporated in MEMS-based actuators to increase the magnitude of the motion generated from these microdevices.[10,11] A similar mechanism can be designed to reduce the displacement experienced by the comb drive in response to a force input. The MEMS sensor proposed in this paper has been designed with a 10:1 displacement reduction mechanism to achieve this goal. When a force is applied vertically onto the top and bottom beams of the sensor, as demonstrated in Fig. 4, the relative motion in the lateral direction between the center mass and the comb-finger sidebars is reduced to $1/10$ of the vertical input displacement.

With the proposed displacement reduction mechanism, the sensitivity of the sensor is substantially improved. The sensitivity of a capacitive force sensor is equal to the change in the capacitance value, C, over the change in the force, F, or displacement, D, input, and thus,

$$Sensitivity = \frac{\partial C}{\partial F} = \frac{\partial C}{\partial D}. \tag{1}$$

The capacitance value of the sensor is inversely related to the initial gap distance and the sensor displacement. With the proposed mechanism design, the sensor displacement in response to a force input is reduced. Hence, it is possible to reduce the initial gap distances by a factor of 10. With this modification, the sensitivity is improved by the same factor as well.
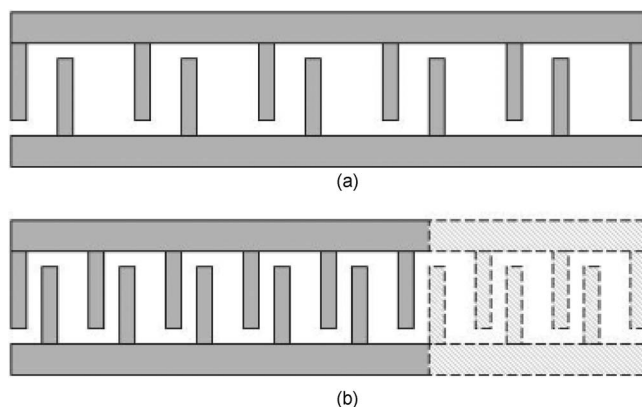
In addition, as the sensor gap distances are reduced, more comb-fingers can be integrated into the design. For this sensor design, it is found that the sensor capacitance as well as the sensor sensitivity can be increased by a factor of 5.7 with this modification. Figure 5 shows a schematic of the improvement made on the comb-drive mechanism design with the displacement reduction mechanism.

The overall sensitivity of the sensor with this reduction mechanism is approximately 57 times higher than the design without the reduction mechanism.

2.4 Sensor Fabrication

The sensor design has been fabricated using a multiuser, silicon-on-insulator (SOI)–based MEMS fabrication process called Micragem.[12] The fabrication process started with a 500-μm-thick glass wafer as the base substrate. The glass surface was patterned and etched to form 10-μm-deep cavities using wet etching. Single crystal silicon (SCSi) with 10-μm thickness was used as the structural layer and was anodically bonded to the glass substrate, leaving only the area above the cavities to be suspended. A thin metal layer was deposited on top of the silicon surface for better electrical conductivity. Last, the sensor structure was patterned and etched using deep reactive ion etching (DRIE). Figure 6 shows an image of the fabricated MEMS sensor under the optical microscope and the sensor parameters are summarized in Table 1.

Table 1 Parameters of the capacitive sensor.

Description	Value
Sensor Dimension	3600 μm $\times$ 1000 μm $\times$ 10 μm
Number of electrodes	118 sets
Electrode length	60 μm
Electrode width	4 μm
Electrode thickness	10 μm
Overlap area	560 μm^2
Nominal gap distance	3 μm and 6 μm
Maximum input displacement	20 μm
Displacement reduction ratio	10:1

Fig. 5 Comb-drive mechanism of (a) the original design and (b) the improved sensor design.

Fig. 7 Detailed view of the comb drive.

Fig. 8 The capacitance value versus gap distance for one set of the comb-finger.
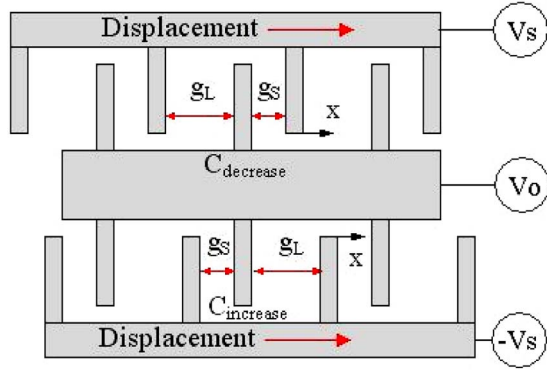
3 Sensor Modeling

3.1 Sensor Capacitance

In space-variation-type capacitive sensors, the capacitance is inversely proportional to the gap that separates the electrodes. The value of the capacitance can be evaluated using the parallel plate equation:

$$C = \frac{\varepsilon A}{g}, \tag{2}$$

where ε is the relative permittivity, A is the overlapping area, and g is the gap distance between the electrodes.

Considering the existence of nonlinear capacitive behavior, the force sensor proposed in this paper employs the use of a differential-style comb-drive configuration. Figure 7 shows a schematic representation of a differential-style comb-drive configuration. The advantage of this type of comb-drive configuration is that for small sensor displacement, nonlinear effects are negligible and a linear relationship between sensor displacement and output capacitance can be achieved.[13]

With the notation in Fig. 7, the capacitance value, $C_{increase}$ and $C_{decrease}$ can be evaluated by considering both gaps g_S and g_L on the two sides of the electrode:

$$C_{increase} = n\left[\frac{\varepsilon A}{(g_S - x)} + \frac{\varepsilon A}{(g_L + x)}\right], \tag{3}$$

$$C_{decrease} = n\left[\frac{\varepsilon A}{(g_S + x)} + \frac{\varepsilon A}{(g_L - x)}\right], \tag{4}$$

where n is the total number of comb-finger sets, g is the initial gap distance on the left and right, and x is the displacement of the sensor.

For this sensor design, the sensor output capacitance is equal to the difference between $C_{increase}$ and $C_{decrease}$. When the sensor is idle, it has a capacitance of zero. The capacitance value increases as a force is applied on the sensor, causing a displacement of the comb-fingers. The relationship between the capacitance value and the gap distance for one set of the comb-finger is plotted in Fig. 8, with the initial gap distances of $g_L = 6$ μm and $g_S = 3$ μm. It is observed that when the sensor displacement is less than
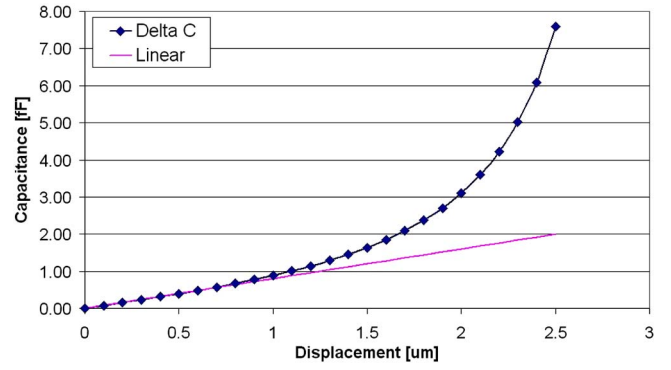
1 μm, the relationship between comb-finger displacement and its resulting capacitance value is relatively linear, with a slope of 0.8 fF/μm, as shown in Fig. 8.

3.2 Spring Constant

In this capacitive sensor, the input force applied on the sensor deforms the sensor. When the input force is small, the relationship between the force and the deformation can be expressed using Hooke's Law:[14]

$$F = kx, \tag{5}$$

where F is the input force, k is the stiffness of the sensor, and x is the deformation.

Simulation from finite element analysis software, COMSOL, shows that the sensor has a stiffness of 537 N/m in the input direction and a stiffness of 4.75 kN/m in the output direction.

3.3 Resonant Frequency

The resonant frequency of the sensor is crucial in determining factors such as the operating bandwidth and is estimated as:

$$\omega_o = \left(\frac{k}{m_{eff}}\right)^{1/2}, \tag{6}$$

where m_{eff} is effective mass of the structure.

The effective mass of the structure represents the actual portion of the overall mass attributed to the structure vibration. For a fixed-fixed cantilever beam, the effective mass can be evaluated as:[15]

$$m_{eff} = \frac{m_L \int_0^L y(x)^2 dx}{y_F^2}, \tag{7}$$

where m_L is mass of the sensor per unit length, y is the displacement of the beam, and y_F is maximum displacement of the sensor.

For the sensor proposed in this paper, the mass of the structure is estimated to be 9.68×10^{-9} kg. The effective mass is calculated to be approximately 0.37 of the overall mass, which is 3.58×10^{-9} kg. The resonant frequency is found to be 61.6 kHz.
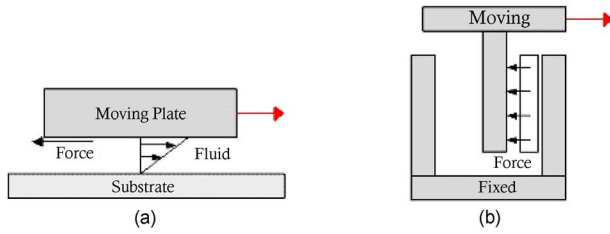
Fig. 9 (a) Slide-film damping and (b) squeeze-film damping.

Fig. 10 Influence of the aspect ratio on the damping constant.

3.4 Damping

Two types of damping mechanisms are active as the comb drives experience displacement: slide-film and squeeze-film damping. Figure 9 illustrates these two damping mechanisms.

Slide-film damping occurs at a result of a sliding motion in a viscous medium. The damping action will exert a damping force against the sliding motion. For the proposed MEMS sensor, slide-film damping occurs at the air gap in between the comb-drive structure and the glass substrate. As the structure displaces, a sliding motion and hence slide-film damping will result. At low frequency, the velocity profile of the fluid underneath the moving plate is linear, and the damping constant is expressed as:[16]

$$b_{slide} = \frac{\mu A}{h}, \tag{8}$$

where μ is the viscosity of medium, A is the area of the sensor mass, and h is the oil layer thickness between the sensor mass and the substrate.

Squeeze-film damping takes place when two parallel plates in a viscous medium displace relative to one another in the normal direction. The lateral movement of the sensor will deflect the comb-fingers and reduce the gap between the comb-fingers. The air within the gap will be squeezed out of the gap to other areas. Due to the air viscosity, an opposing force is generated with the force proportional to the velocity of the sensor mass. For a small comb-finger deflection, the squeeze-film damping constant can be calculated as:[17]

$$b_{squeeze} = \frac{\mu \alpha(W/L) L W^3}{g^3}, \tag{9}$$

where W and L are the width and length of the comb-finger, and $\alpha(W/L)$ is a function of the aspect ratio of the finger. The value of $\alpha(W/L)$ can be obtained from Fig. 10 based on the width and length of the comb-finger.[17]

The total damping factor of the sensor, b, is equal to the sum of the squeeze-film and slide-film damping:

$$b = b_{slide} + b_{squeeze}. \tag{10}$$

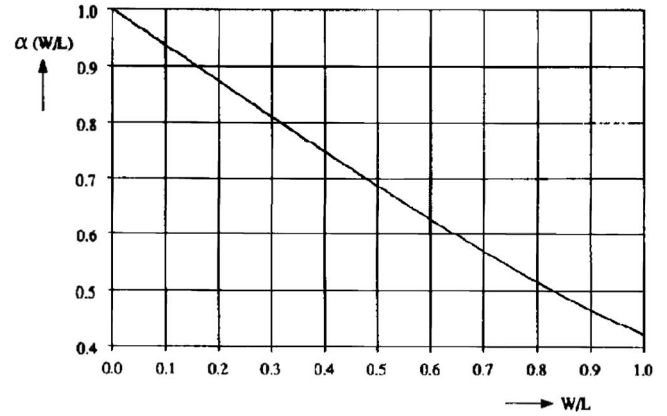At a temperature of 25 °C, the sensor has a total damping factor of 3.15×10^{-6} Ns/m.

3.5 Quality Factor

The quality factor, Q, is the ratio between the total energy stored in the system to the energy lost per cycle due to the damping effects present. The quality factor of the system is given as:[18]

$$\frac{1}{Q} = \frac{1}{Q_a} + \frac{1}{Q_s} + \frac{1}{Q_i}, \tag{11}$$

where Q_a is the energy lost to the surrounding fluid, Q_s is the energy dissipated through the supports to the surrounding solid, and Q_i is the energy dissipated within the internal structure.

The energy lost to the surrounding fluid is found to be the dominant factor in the sensor design and is evaluated as:

$$Q = \frac{k}{\omega_o b}. \tag{12}$$

The calculated quality factor of the sensor is approximately 440.

4 Readout Circuit

A schematic of the capacitance readout circuit is presented in Figure 11. The circuit utilizes a differential charge amplifier, taken from Ref. 19, and a voltage comparator with a variable resistor to generate an on or off signal to the vehicle battery supply system. The differential charge amplifier in the readout circuit converts the sensor capacitance to an electrical voltage. A sinusoidal voltage input of 2 Vp-p, 60 kHz is connected to the capacitive sensor, C_{sensor}. A high-frequency input signal is selected as the power source of the sensor to minimize the noise within the input signal.[20] A replica of this sinusoidal input is phase-shifted 180 deg using an inverting amplifier to generate another voltage input to the reference capacitor, C_{ref}. The voltage output of the charge amplifier, V_{out}, is then calculated as:[19]

$$V_{out} = \frac{(C_{sensor} - C_{ref})}{C_{dem}} V_{in}, \tag{13}$$

where C_{dem} is the capacitance value across the charge amplifier.
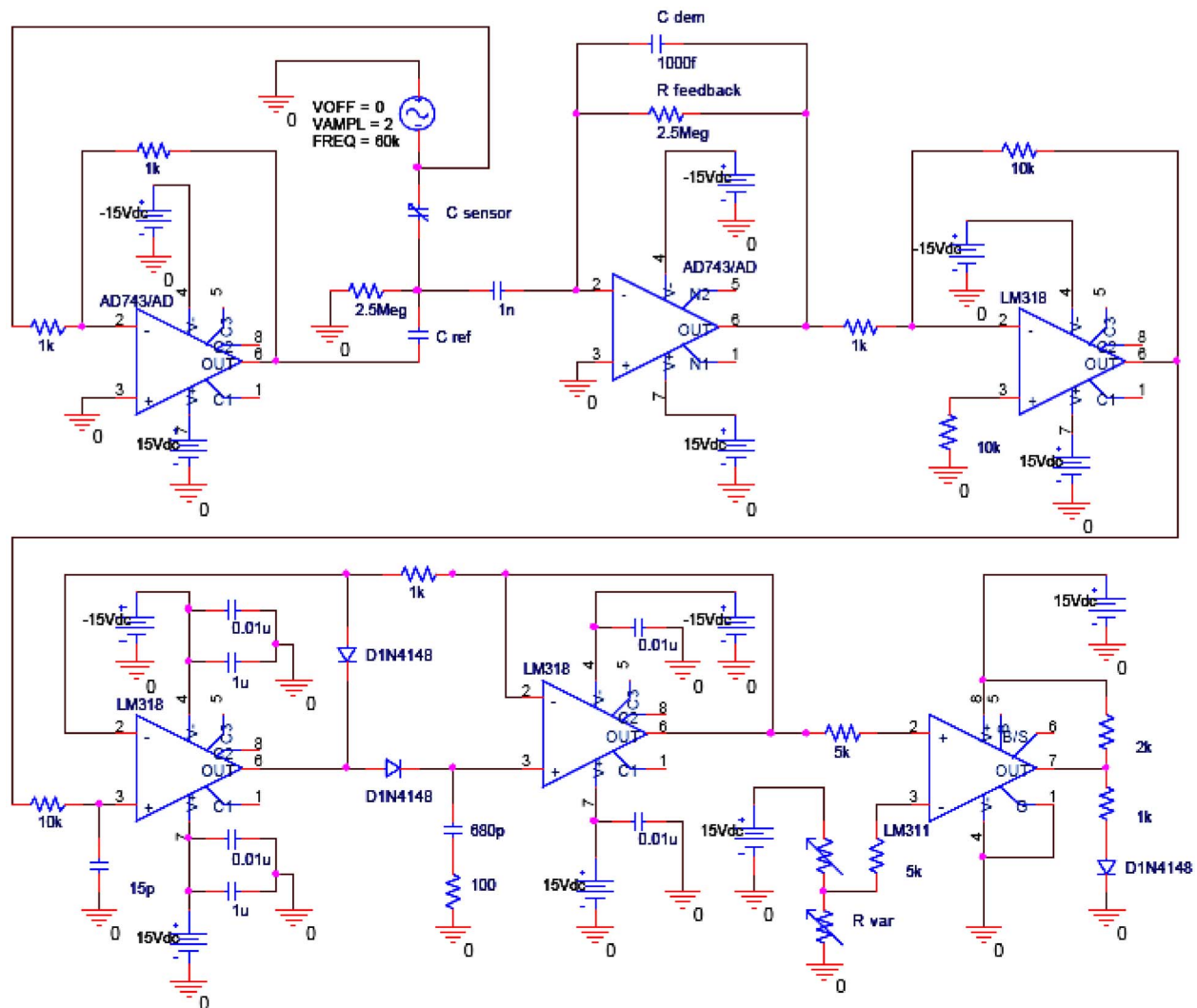
Fig. 11 Schematic of the readout circuit.

According to Eq. (13), a small capacitance should be used for C_{dem} in order to maximize the voltage output of the charge amplifier. In this design of the readout circuit, a 1-pF capacitor is selected as the C_{dem}. The 1-nF capacitor and the 2.5-MΩ resistor in front of the charge amplifier are to block away any DC voltage in the signal into the charge amplifier.[19,21] A feedback resistor of 2.5 MΩ is used to prevent saturation of the charge amplifier.[19,22]

The voltage output from the charge amplifier is then amplified by a gain factor of 11 through the following non-inverting amplifier. The amplified voltage is then passed to a peak detector design, taken from Ref. 23. The peak detector determines the peak value of the sinusoidal voltage and outputs a steady DC voltage at this peak value. This DC voltage will be compared to another voltage from a variable resistor at the voltage comparator. The variable resistor allows adjustment on the threshold voltage of the voltage comparator. The output from the entire readout circuit is normally an on signal. When the voltage from the peak detector increases and exceeds the threshold value as

a result of an external force imparted onto the sensor, an off signal will be generated to notify the battery power system to terminate the power supply.

A prototype of the readout circuit was fabricated using the conventional printed circuit board (PCB) fabrication process. The PCB is a double-layered board with a 0.062-in. FR-4 laminate as the board material. It has an overall dimension of 3.5 in. by 2.5 in. and has an LED to indicate the on and off signals of the board output. The sensitivity of this circuit, using Eq. (13) with an amplification factor of 11, is calculated to be 22 V/pF.

5 Noise Analysis

System noise affects the overall performance of the sensor. Since MEMS devices are very small and compact, the output signal is usually low. The signal-to-noise ratio of the system has an impact on factors such as the minimum detectable signal of the sensor.
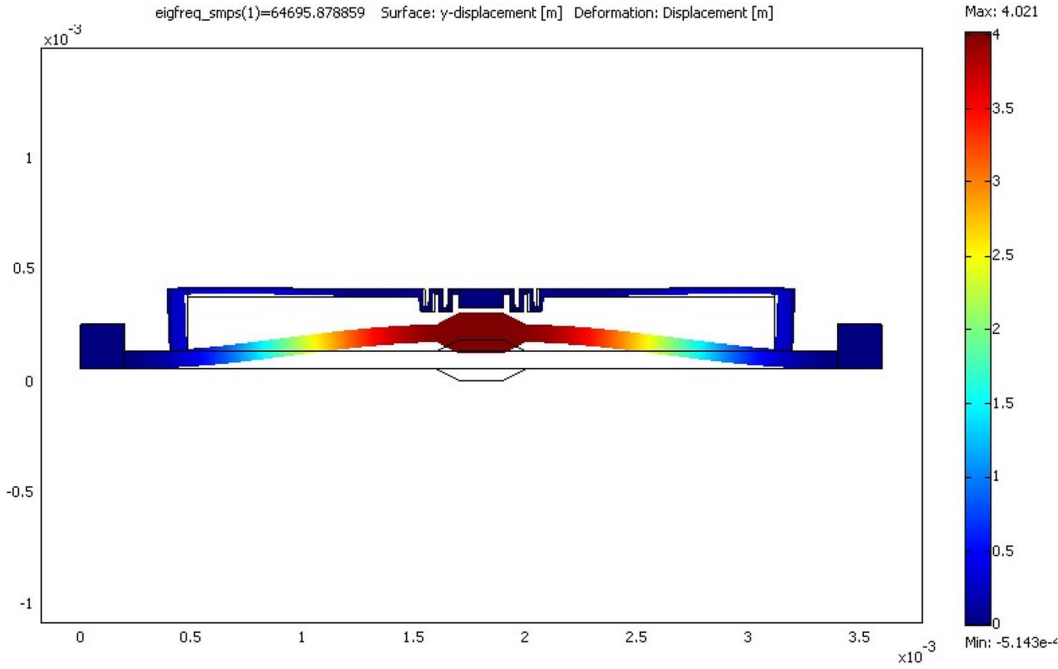
Fig. 12 First-mode resonant frequency of the sensor.

5.1 Noise in the Sensor

The thermodynamics noise, or the Johnson-Nyquist noise, is one of the noise sources in the MEMS sensor. This noise is due to the energy dissipation of the thermal energy stored within the mechanical structure. The resultant noise-induced displacement on the sensor structure can be evaluated using the Brownian noise equation:[24,25]

$$\overline{X_n^2} = \frac{4k_B T b}{k^2}\left[\frac{1}{1-(\omega/\omega_o)^2+(\omega/Q\omega_o)^2}\right], \tag{14}$$

where k_B is the Brownian constant, 1.38×10^{-23} Nm/K, and T is the temperature.

For sensors to be operated well below the resonant frequency, the Brownian noise equation can be simplified as:

$$\overline{X_n^2} = \frac{4k_B T b}{k^2} = \frac{4k_B T}{w_o Q k}. \tag{15}$$

The resonant frequency of the sensor was simulated using COMSOL. Considering the sensor structure as a lumped cantilever beam, the first-mode resonant frequency was found to be 61 kHz, as shown in Fig. 12. The equivalent noise level at this frequency for a Q factor of 440 and at room temperature 298 K was determined to be 4.24×10^{-16} m/Hz$^{1/2}$. Since the displacement of the comb-drive mechanisms are 1/10 of the sensor displacement, the equivalent noise level of the comb drive is approximately 0.43×10^{-16} m/Hz$^{1/2}$, which is equivalent to a voltage noise level of 0.088 nV/Hz$^{1/2}$.

5.2 Noise in the Readout Circuit

At the low-frequency region, flicker noise or $1/f$ noise is the dominating noise source. Flicker noise is present in all materials used in electronics and can be evaluated by the following equation:[26]

$$Noise_{Flicker} = \left(K^2 \ln\frac{f_H}{f_L}\right)^{1/2}, \tag{16}$$

where K is the normalized device constant at 1 Hz, and f_H and f_L are the lowest and highest frequency of the bandwidth.

If the input voltage noise spectral density of the component is known, the K value can be evaluated using the following equation:[27]
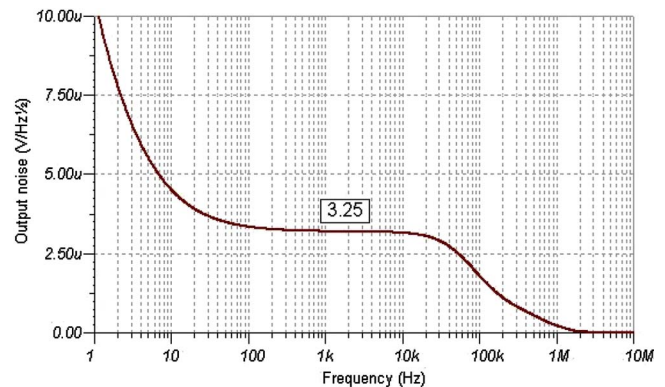

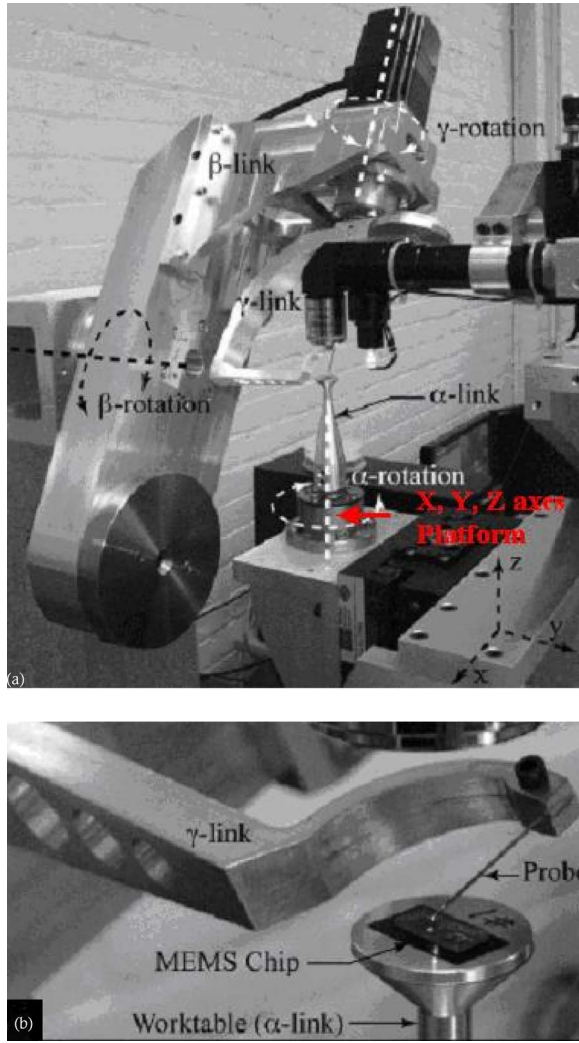**Fig. 13** Simulation result of the voltage noise spectral density.

Fig. 14 The 6-DOF manipulator in the experiment: (a) overall view; (b) close-up view of the sensor on the platform stand.

Fig. 15 The sensor packaged on a PGA.

$$K^2 = (e_L^2 - e_F^2)(f_L), \qquad (17)$$

where e_L is the noise voltage at lowest possible frequency in the $1/f$ noise region at frequency f_L, and e_F is the white or flat noise voltage.

Using Eq. (17), the K values of the operational amplifiers, AD-743, are calculated to be 24.8 nV.

Similar to the sensor structure, thermal noise also exists in all resistive elements within the readout circuit. The level of noise is proportional to the temperature as well as the resistance value. At frequencies below 100 MHz, the thermal noise can be estimated with the following equation:[26]

$$e_{Thermal} = (4k_B TR)^{1/2}, \qquad (18)$$

where R is the resistance value in ohms.

For the readout circuit proposed in this work, the thermal noise from the two 2.5-MΩ resistors in the charge amplifier is determined to be the most significant. The flicker noise in the circuit is comparatively small and is neglected from the calculation. Each resistor has a noise level of 202 nV/Hz$^{1/2}$. Adding the two noncorrelated noise
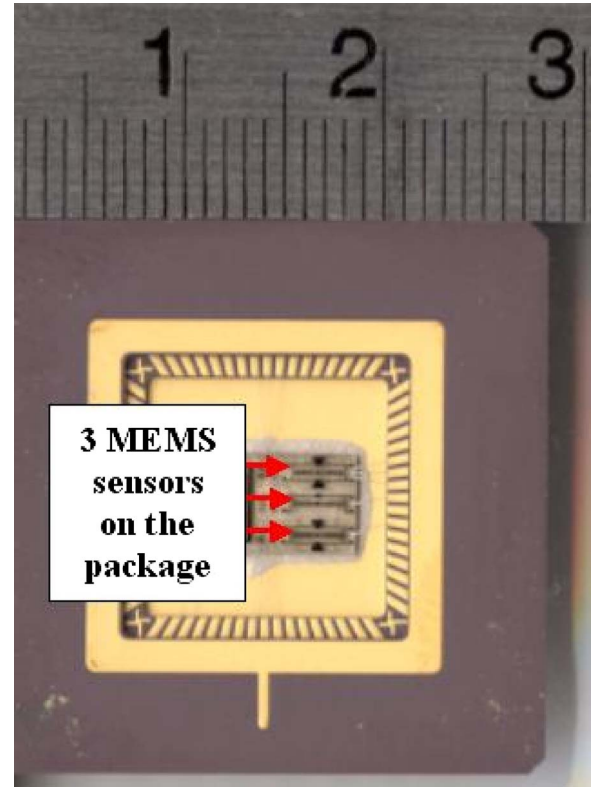
sources together, a total noise level of 290 nV/Hz$^{1/2}$ is estimated. This noise signal will be amplified as it passes through the noninverting amplifier, which has a gain factor of 11. As a result, output noise is expected to be about 3190 nV/Hz$^{1/2}$. Simulation results from TINA-TI software in Fig. 13 show that the noise floor of the sensing circuit is about 3250 nV/Hz$^{1/2}$ or 3.25 μV/Hz$^{1/2}$, which is very close to the noise level computed from the previously mentioned equations and correlations.

6 Experimental Results

6.1 Sensor Capacitance

Figure 14 shows the manipulator and the tungsten probe with a tip radius of 25 μm used in the experiment.[28] The sensor was wire-bonded onto a standard ceramic pin guide array (PGA), as shown in Fig. 15. The packaged sensor was mounted onto the movable platform of the manipulator during the experiment. The movable platform has a resolution of 0.2 μm in the x-, y-, and z-axis directions.[28] The sensor was pushed toward the probe tip to emulate a force input onto the sensor. Corresponding to a 1-mm displacement of the sensor toward the probe is an input force of 537 μN applied to the sensor. A capacitance-to-digital converter board (Model AD7746, Analog Devices) was connected to the sensor to measure the change in the capacitance at different loading conditions. For every measurement, 100 data points were sampled, and the peak-to-peak variation was measured to be less than 5 fF. The capacitance values were transferred to a desktop computer for analysis. Experimental results and the theoretical prediction are plotted in Fig. 16. For a 20-μm displacement, a 188-fF change in the ca-
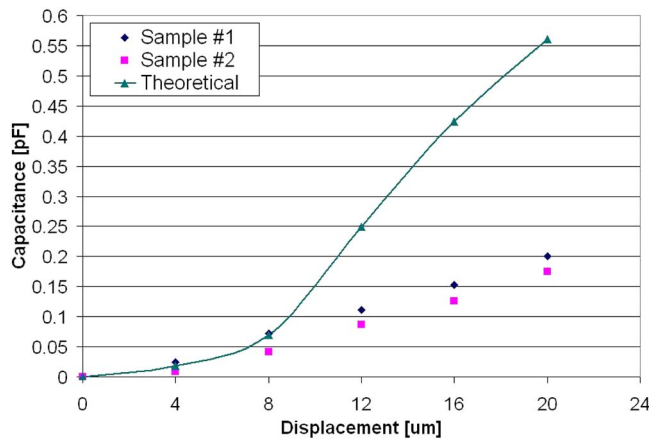
Fig. 16 Capacitance response of the MEMS force sensor.

Fig. 18 Voltage output of different capacitors.

pacitance value was measured, whereas a change of 500-fF capacitance is expected from the theoretical equation. The discrepancy between two values may be due to out-of-plane displacement in the comb drive, which results a reduction in the overlapping area. One possible solution to minimize the effect is to use flexure hinges to ensure that the deflections are in the planar direction.[29] Inherent parasitic capacitance within the sensor and the testing equipment may also be another error source for the discrepancy in the output capacitance of the sensor.

6.2 *Readout Circuit Output*

To evaluate the performance of the readout circuit, capacitors with known values were connected to the readout circuit. The voltage output after the charge amplifier was measured using an HP54600 oscilloscope. Fig. 17 shows the voltage output for a 4-pF capacitor after the readout circuit. The measured capacitance-voltage response of the readout circuit for a series of capacitors was plotted in Fig. 18. It is found that a relatively linear relationship between the capacitance and the voltage output can be achieved with the readout circuit, providing a sensitivity of approximately 1.45 V/pF. The theoretical sensitivity calculated using Eq. (13) is approximately 2 V/pF. The discrepancy between two values is mainly due to the existence of parasitic capacitance in the operational amplifier and in the circuit
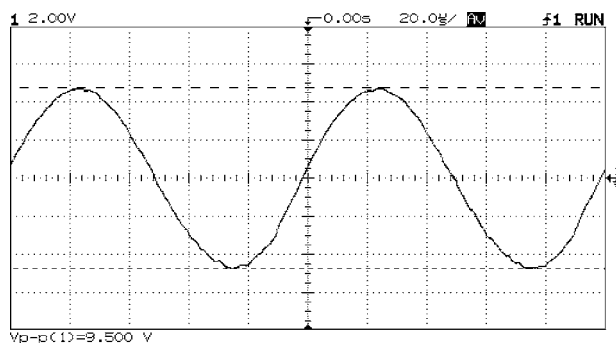
board. Since a small value of C_{dem} is selected, the parasitic capacitance will increase C_{dem} and hence lower the sensitivity of the circuit.

The noise level of the sensing circuit was measured using an HP/Agilent 35670A Dynamic Signal Analyzer. The voltage noise spectral density of the circuit was plotted on Fig. 19. The noise floor was measured to be 5.21 $\mu V/Hz^{1/2}$, compared to the calculated noise of 3.25 $\mu V/Hz^{1/2}$. For an operating bandwidth of 1 kHz, the noise voltage will be about 164 μV. Hence, the equivalent minimum detectable capacitance of the readout circuit is approximately 0.07 fF.

7 Conclusion

A power disconnect proposed for use with 42-V automotive power systems is presented in this paper. The design aims to prevent arc discharge during the disconnection of such high-voltage systems. This power disconnect, integrated with a MEMS-based force sensor, will terminate the power supply when a service technician disconnects the connectors. A space-variation type capacitive sensor is selected as
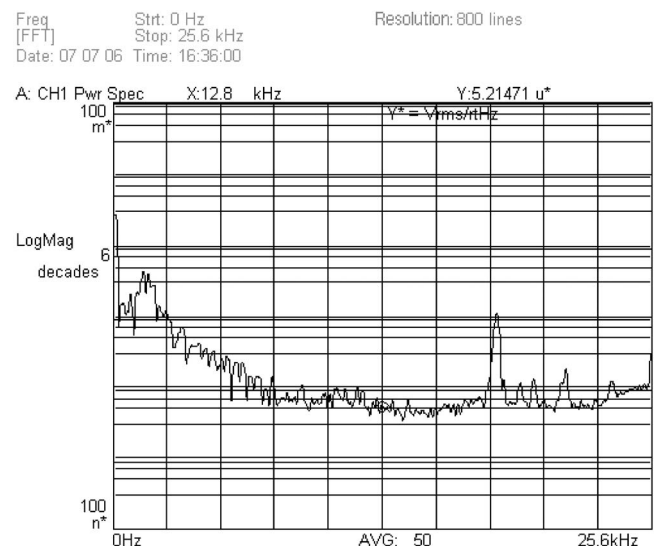

Fig. 19 Experimental result of the voltage noise spectral density.

Fig. 17 Oscilloscope output of the readout circuit with a 4-pF capacitor.

the force sensing mechanism. This sensor design incorporates a displacement reduction mechanism to increase the sensitivity of the sensor. Results show that a 10:1 displacement reduction ratio can be achieved and the sensitivity can be improved by 57 times with the mechanism. When a $20\text{-}\mu$m displacement, or a 10.7-mN force, is applied on the sensor, the capacitance output is measured to be 188 pF. A readout circuit is designed to convert the capacitance change to voltage and to generate the off signal to terminate the power supply when the voltage exceeds the preset threshold. This circuit board has a sensitivity of 15.95 V/pF after amplification, and the noise floor is measured to be 5.21 μV/Hz$^{1/2}$.

Acknowledgments

References

1. A. Graf, "Semiconductors in the 42 V PowerNet," presented at the *42 V Automotive Systems Conference*, Chicago, 17–18 September 2001, Intertech Corp., Portland, ME (2001).
2. A. Jahed, A. Housely, and J. Spoonhower, SEMA 42-volt systems overview, Specialty Equipment Market Association (SEMA) (2002).
3. R. Dixon and J. Bouchaud, "Prospects for MST sensors in automotive," in *Advanced Microsystems for Automotive Applications*, J. Valldorf and W. Gessner, Eds., pp. 3–12, Springer, Berlin, Heidelberg (2006).
4. H. K. Chu, J. K. Mills, and W. L. Cleghorn, "Stereolithography as a meso-structure for input force reduction to a capacitive force MEMS sensor," *Proc. SPIE* **6464**, 64640Q (2007).
5. L. K. Baxter, *Capacitive Sensors: Design and Applications*, IEEE Press Series on Electronics Technology, R. J. Herrick, Ed., John Wiley & Sons, New York (1997).
6. M. Despont, G. A. Racine, P. Renaud, and N. F. de Rooij, "New design of micromachined capacitive force sensor," *J. Micromech. Microeng.* **3**, 239–242 (1993).
7. Y. Sun, B. J. Nelson, D. P. Potasek, and E. Enikov, "A bulk microfabricated multi-axis capacitive cellular force sensor using transverse comb drives," *J. Micromech. Microeng.* **12**, 832–840 (2002).
8. J. Aebersold, K. Walsh, M. Crain, M. Martin, M. Voor, J.-T. Lin, D. Jackson, W. Hnat, and J. Naber, "Design and development of a MEMS capacitive bending strain sensor," *J. Micromech. Microeng.* **16**, 935–942 (2006).
9. H. K. Chu, J. K. Mills, and W. L. Cleghorn, "Design of a high sensitivity capacitive force sensor," in *7th IEEE International Conference on Nanotechnology* (2007) (in press).
10. N. Lobontiu and E. Garcia, "Analytical model of displacement amplification and stiffness optimization for a class of flexure-based compliant mechanisms," *Comput. Struct.* **81**, 2797–2810 (2003).
11. E. Garcia, Y. Nam, and N. Lobontiu, "Design, modeling, and initial experiments on microscale amplification device," *J. Intell. Mater. Syst. Struct.* **16**, 1039–1049 (2005).
12. CMC Microsystems and Micralyne, "Introduction to micragem: a silicon-on-insulator based micromachining process," Report ICI-138 V4.0, CMC Microsystems and Micralyne (2005).
13. A. S. Tamsir F. Saharil, and B. Y. Majlis, "Finger beam geometrical behavior analysis of a non-crossing differential capacitive MEMS accelerometer," *Proc. Intl. Conf. Software Engg.* 673–676 (2004).
14. J. Shigley, *Mechanical Engineering Design*, 7th ed., pp. 72–104, McGraw Hill, New York (2003).
15. J. Brotz, "Damping in CMOS-MEMS Resonator," MASc Dissertation, Dept. Electrical and Computer Engineering, Carnegie Mellon University, Pittsburgh (2004).
16. Y. H. Cho, B. M. Kwak, A. P. Pisano, and R. T. Howe, "Slide film damping in laterally driven microstructures," *Sens. Actuators, A* **40**, 31–39 (1994).
17. R. P. van Kampen, M. J. Vellekoop, P. M. Sarro, and R. F. Wolffenbuttel, "Application of electrostatic feedback to critical damping of an integrated silicon capacitive accelerometer," *Sens. Actuators, A* **43**, 100–106 (1994).
18. S. Beeby, *MEMS Mechanical Sensors*, pp. 85–112, Artech House, Boston, (2004).
19. M. Kraft, "Closed loop digital accelerometer employing oversampling conversion," PhD Dissertation, School of Engineering, Coventry University, UK (1997).
20. N. Yazdi, H. Kulah, and K. Najafi, "Precision readout circuit for capacitive microaccelerometers," in *Proc. IEEE Sensors 2004*, D. Rocha, P. M. Sarro, and M. J. Vellekoop, Eds., pp. 28–31 (2004).
21. B. E. Boser, "Electronics for micromachined inertial sensors," in *Int. Conf. Solid-State Sensors and Actuators*, Vol. **2**, pp. 1169–1172 (1997).
22. W. J. Smith and J. R. LaCourse, "Non-contact biopotential measurement from the human body using a low-impedance charge amplifier," *Proc. IEEE 30th Annual Northeast Bioengineering Conference*, Vol. **30**, pp. 31–32 (2004).
23. Analog Devices, "AD843 Datasheet," Rev. D, Analog Devices Inc., Norwood, MA (2006).
24. G. M. Rebeiz, *RF MEMS Theory, Design, and Technology*, pp. 429–448, John Wiley and Son, Hoboken, NJ (2003).
25. M. Suster, J. Guo, N. Chaimanonart, W. H. Ko, and D. J. Young, "A high-performance MEMS capacitive strain sensing System," *J. Microelectromech. Syst.* **15**(5), 1069–1077 (2006).
26. B. Carter, "Op-amp noise theory and applications," in *Op Amps for Everyone*, Texas Instruments Literature No. SLOA082, Texas Instruments, Inc., Dallas (2001).
27. "Noise analysis in operational amplifier circuits–application report," Texas Instruments Literature No. SLVA043B (2007).
28. N. Dechev, L. Ren, W. Liu, W. L. Cleghorn, and J. K. Mills, "Development of a 6 degree of freedom robotic micromanipulator for use in 3D MEMS Microassembly," in *Proc. 2006 IEEE Int. Conf. Robotics and Automation*, pp. 281–288 (2006).
29. N. Lobontiu, J. S. N. Paine, E. Garcia, and M. Goldfarb, "Corner-filleted flexure hinge," *J. Mech. Des.* **123**(3), 346–352 (2001).
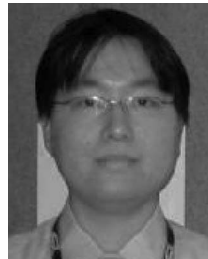
Henry K. Chu received a BASc degree in mechanical engineering from the University of Waterloo, Ontario, Canada, in 2005. He is currently working toward an MASc degree in mechanical and industrial engineering at the University of Toronto. His research interests include MEMS force sensor and packaging design for automotive applications.

James K. Mills received bachelor's and master's degrees in electrical engineering in 1980 and 1982, respectively, and a PhD degree in mechanical engineering in 1987 from the University of Toronto, Ontario, Canada. He is currently a professor of mechanical engineering at the University of Toronto, and his research interests have encompassed a number of related areas, including robot control, control of multirobots, control of flexible link robots, design of actuators, localization, development of fixtureless assembly technology, design and control of high-speed machines, and development of neural network controllers. He has published over 220 journal and conference papers and supervised over 55 master's and PhD students and a number of postdoctoral fellows and research engineers. He has been an invited visiting professor at the Centre for Artificial Intelligence and Robotics in Bangalore, India, in 1997 and the Hong Kong University of Science and Technology in 1995. More recently, he was a visiting professor in the Department of Automation and Computer Aided Engineering at the Chinese University of Hong Kong from 2002 to 2003.
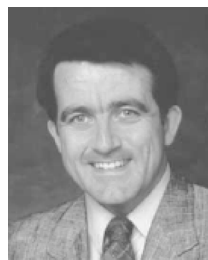
William L. Cleghorn received a BASc degree in 1975, an MASc degree in 1976, and a PhD degree in 1980, all from the University of Toronto, Ontario, Canada, Department of Mechanical Engineering. He is currently a professor in the same department, and his current areas of research include dynamics, vibrations, and mechanisms. He has published over 200 journal and conference papers in these areas. He currently holds the Clarice Chalmers Chair of Engineering Design.